Imprint of a nuclear bubble in nucleon-nucleus diffraction

V. Choudhary [1,*] W. Horiuchi [2,†] M. Kimura,[2,3,‡] and R. Chatterjee[1,§]

[1]*Department of Physics, Indian Institute of Technology Roorkee, Roorkee 247 667, India*
[2]*Department of Physics, Hokkaido University, 060-0810 Sapporo, Japan*
[3]*Nuclear Reaction Data Centre, Faculty of Science, Hokkaido University, 060-0810 Sapporo, Japan*

Background: The density of most nuclei is constant in the central region and is smoothly decreasing at the surface. A depletion in the central part of the nuclear density can have nuclear structure effects leading to the formation of "bubble" nuclei. However, probing the density profile of the nuclear interior is, in general, very challenging.

Purpose: The aim of this paper is to investigate the nuclear bubble structure, with nucleon-nucleus scattering, and quantify the effect that the bubble structure has on the nuclear surface profile.

Method: We employed high-energy nucleon-nucleus scattering, using the Glauber model to analyze various reaction observables, which helps in quantifying the nuclear bubble. The effectiveness of this method is tested on ^{28}Si with harmonic-oscillator (HO) densities, before applying it on even-even $N = 14$ isotones, in the $22 \leqslant A \leqslant 34$ mass range, with realistic densities obtained from antisymmetrized molecular dynamics (AMD).

Results: Elastic scattering differential cross sections and reaction probability for the proton-^{28}Si reaction are calculated using the HO density to design tests for signatures of the nuclear bubble structure. We then quantify the degree of bubble structure for $N = 14$ isotones with the AMD densities by analyzing their elastic scattering at 325, 550, and 800 MeV incident energies. The present analyses suggest ^{22}O as the most measurable candidate for a bubble nucleus, among even-even $N = 14$ isotones, in the $22 \leqslant A \leqslant 34$ mass range.

Conclusion: We have shown that the bubble structure information is imprinted on the nucleon-nucleus elastic scattering differential cross section, especially in the first diffraction peak. Bubble nuclei tend to have a sharper nuclear surface and deformation seems to be a hindrance in their emergence.

I. INTRODUCTION

Advances of radioactive beam facilities have allowed us to study nuclei with extreme neutron to proton ratios. In fact, close to the neutron drip line, exotic features such as the halo [1,2]—an extended low density tail in the neutron matter distribution—have been discovered. At least for light nuclei, this was thought to be a threshold phenomenon resulting from the presence of a loosely bound state near the continuum. In this context, with current interest moving towards the medium mass region, another exotic structure—that of a depression in the central part of nuclear density, called a "bubble"—has attracted considerable attention.

Systematic studies of electron scattering on stable nuclei have revealed that the central density of stable nuclei is almost constant, $\rho_0 \approx 0.16$ fm^{-3} [3]. In light nuclei, distinct nuclear orbitals play a role in the emergence of the bubble structure. If the s orbitals are empty, the interior density of nuclei becomes depleted. For example, using several mean-field approaches

Refs. [4,5] showed that the central depression of the proton density in ^{34}Si is about 40% as compared to stable ^{36}S, originating from the proton deficiency in the $1s_{1/2}$ orbit. The possibilities of forming bubble nuclei have also been explored theoretically in the medium [4,6–11] and superheavy mass regions [12,13].

The experimental indication of the central depression of protons in the unstable nucleus ^{34}Si was recently reported using γ-ray spectroscopy [14]. Electron scattering on unstable nuclei is the most direct way to probe the central depression of proton density in bubble nuclei. Recently, the SCRIT electron scattering facility at RIKEN has succeeded in extracting information about the nuclear shape of ^{132}Xe [15].

However, unlike a hadronic probe, which is sensitive to both neutrons and protons, electron scattering poses difficulties for probing the neutron density distribution even for stable nuclei [16]. In this context, it is worth mentioning that proton-nucleus scattering has been successfully applied to deduce the nuclear matter density distributions [17]. Proton scattering can also be extended for unstable nuclei with the use of inverse kinematics measurement, as demonstrated in Ref. [18]. Indeed, this motivates us to inquire if information on the bubble structure in nuclei can be investigated with nucleon-nucleus scattering.

---
*vchoudhary@ph.iitr.ac.in
†whoriuchi@nucl.sci.hokudai.ac.jp
‡masaaki@nucl.sci.hokudai.ac.jp
§rchatterjee@ph.iitr.ac.in

In this paper, we perform a systematic study to test nucleon-nucleus scattering as a probe of the nuclear bubble structure. This paper is organized as follows. Section II briefly presents the formalism that describes the nucleon-nucleus collision at high incident energy within the Glauber model, wherein the elastic scattering and total reaction cross sections are evaluated. Using this formulation, in Sec. III we discuss how signatures of the nuclear bubble structure are reflected in the cross sections by using an example of a simple ideal case, ^{28}Si. We show the relationship between the internal depression and the surface diffuseness, and propose a practical way to evaluate the bubble structure. For this purpose, the generalized "bubble" parameter is introduced as a measure of the nuclear bubble structure. In this work, we also examine the structure of $N = 14$ isotones, ^{22}O, ^{24}Ne, ^{26}Mg, ^{28}Si, ^{30}S, ^{32}Ar, and ^{34}Ca. Section IV presents details of the structure calculation by the antisymmetrized molecular dynamics (AMD) model. The formalism is briefly explained in Sec. IV A, and the resulting structure information focusing on the bubble structure is given in the following Sec. IV B. Section V demonstrates how the nucleon-nucleus scattering works for extracting the bubble parameter of the nuclear density distributions. We discuss the feasibility through a systematic analysis of the elastic scattering differential cross sections with various density profiles. The conclusions of our study are presented in Sec. VI. Some details on how nuclear structure parameters are evaluated in the AMD are in the Appendix.

II. NUCLEON-NUCLEUS REACTIONS WITH GLAUBER MODEL

The Glauber theory offers a powerful description of high-energy nuclear reactions [19]. Here we consider the normal kinematics in which the incident proton is bombarded on a target nucleus. Thanks to the eikonal and adiabatic approximations, the final state wave function of the target nucleus after the collision is simplified as

$$|\phi_f\rangle = e^{i\chi}|\phi_i\rangle, \tag{1}$$

where $|\phi_i\rangle$ represents the initial wave function of the target nucleus, and $e^{i\chi}$ is the phase-shift function, which includes all the information about the nucleon-nucleus collision. The elastic scattering amplitude for the nucleon-nucleus reaction is given by

$$F(\mathbf{q}) = \frac{iK}{2\pi} \int d\mathbf{b}\, e^{i\mathbf{q}\cdot\mathbf{b}} \left(1 - e^{i\chi_N(\mathbf{b})}\right), \tag{2}$$

where K is the relative wave number of the incident nucleon, $\mathbf{b}$ is the impact parameter vector perpendicular to the beam direction, and $\mathbf{q}$ is the momentum transfer vector of the incident nucleon. With this scattering amplitude, the elastic scattering differential cross section can be evaluated by

$$\frac{d\sigma}{d\Omega} = |F(\mathbf{q})|^2. \tag{3}$$

The total reaction cross section of the nucleon-nucleus collision can be calculated by

$$\sigma_R = \int d\mathbf{b}\, P(\mathbf{b}) \tag{4}$$

with the nucleon-nucleus reaction probability defined as

$$P(\mathbf{b}) = 1 - \left|e^{i\chi(\mathbf{b})}\right|^2. \tag{5}$$

Since the evaluation of the phase-shift function is demanding in general, for the sake of simplicity we employ the optical-limit approximation (OLA). As presented in Refs. [20–23], the OLA works well for many cases of proton-nucleus scattering, so the multiple scattering effects can be ignored. The optical phase-shift function for the nucleon-nucleus scattering in the OLA is given by

$$e^{i\chi_N(\mathbf{b})} \approx \exp\left[-\int d\mathbf{r}\, \rho_N(\mathbf{r})\Gamma_{NN}(\mathbf{b}-\mathbf{s})\right], \tag{6}$$

where $\mathbf{r} = (\mathbf{s}, z)$, and $\mathbf{s}$ is the two-dimensional vector perpendicular to the beam direction z. $\rho_N(\mathbf{r})$ denotes the nucleon density distributions measured from the center of mass of the system. The crux of any calculation will be to calculate this density with reliable nuclear structure models. This is also the primary point where information on the bubble structure enters into the Glauber model and is reflected in the scattering or reaction observables.

Γ_{NN} is the profile function, which describes the nucleon-nucleon collisions. The profile function for the nucleon-nucleon scattering is usually parametrized as given in Ref. [24]:

$$\Gamma_{NN}(\mathbf{b}) = \frac{1 - i\alpha_{NN}}{4\pi\beta_{NN}} \sigma_{NN}^{\text{tot}} \exp\left(-\frac{\mathbf{b}^2}{2\beta_{NN}}\right), \tag{7}$$

where α_{NN} is the ratio of the real part to the imaginary part of the nucleon-nucleon scattering amplitude in the forward direction, β_{NN} is the slope parameter of the differential cross section, and σ_{NN}^{tot} is the nucleon-nucleon total cross section. Standard parameter sets of the profile function are listed in Refs. [25,26].

III. HOW IS NUCLEAR BUBBLE STRUCTURE REFLECTED?

In this section, we discuss how the nuclear bubble gets reflected in the proton-nucleus scattering at high incident energies, where the Glauber model works fairly well. For the sake of simplicity, we use the averaged NN profile function given in Ref. [25] and ignore the Coulomb interaction. Note that the difference between the pp and pn cross sections in the profile functions can be neglected in the total reaction cross section calculations at the incident energy of $E \gtrsim 300$ MeV [21].

A. Density distribution of ^{28}Si

Here, we discuss the density distribution of ^{28}Si within the harmonic-oscillator (HO) model. First, we consider two types of configurations, $(0d)^{12}$ and $(0d)^8(1s)^4$, and calculate their density distributions with the center-of-mass correction [22], which are denoted as $\rho^d(r)$ and $\rho^s(r)$, respectively. Note that $\rho^d(r)$ shows the most prominent bubble structure because of the vacancy of the $1s$ orbit, while $\rho^s(r)$ does not. Then, we interpolate these two densities as

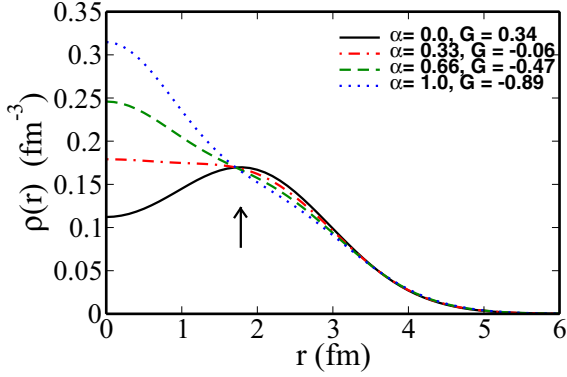$$\rho(\alpha; r) = (1-\alpha)\rho^d(r) + \alpha\rho^s(r), \tag{8}$$

FIG. 1. Matter density distributions of ^{28}Si with various bubble parameters (G). The arrow indicates the reference radius, 1.8 fm. See text for more details.

where the mixing parameter α ($0 \leqslant \alpha \leqslant 1$) controls the occupation probability of the $1s$ orbit. Consequently, $\alpha = 0$ yields the most bubbly density, whereas $\alpha = 1$ yields nonbubble density. For a given value of α, the size parameter of HO is chosen to reproduce the observed point-proton root-mean-square rms radius, 3.01 fm [27].

To quantify a degree of "bubble," we introduce the bubble parameter (G) as

$$G = \frac{\rho(D) - \rho(0)}{\rho(D)}, \qquad (9)$$

where D denotes the reference radius at which the $\rho^d(r)$ or $\rho(\alpha = 0; r)$ takes its maximum value. In the case of ^{28}Si, $D = 1.8$ fm. $\rho(0)$ and $\rho(D)$ represent the densities at $r = 0$ and D, respectively. We remark that this is an extension of the bubble parameter (depletion fraction) given in Ref. [4], where it is defined only by positive values. This extension enables us to quantify the degree of the bubble structure for any nuclear density distribution irrespective of whether it exhibits a bubble or not.

Figure 1 displays how the matter density distribution of ^{28}Si and the corresponding G value change depending on the mixing parameter α. In the present case of ^{28}Si, the values of G range from 0.34 ($\alpha = 0$) to -0.89 ($\alpha = 1$), allowing for negative values which signify that the central density is higher than the density at the reference radius. Apparently, the bubble degree is maximized at $G = 0.34$ with $\alpha = 0$, which clearly exhibits a strong depression of the central density, thereby suggesting the bubble structure. The value of G decreases with increasing mixing of the $1s$ orbits. An almost flat behavior of the density distribution ($G \approx 0$) is obtained with $\alpha = 0.33$.

In the same manner, we construct the model densities for other $N = 14$ isotones from ^{22}O to ^{34}Ca. We calculate $\rho^d(r)$ and $\rho^s(r)$ as the density distributions of the $(0d)^{A-16}$ and $(1s)^4(0d)^{A-20}$ configurations with $22 \leqslant A \leqslant 34$. These two densities are interpolated as in Eq. (8) and used for the reaction calculation in the following sections. The reference radius D and the bubble parameters are also defined in the same way.
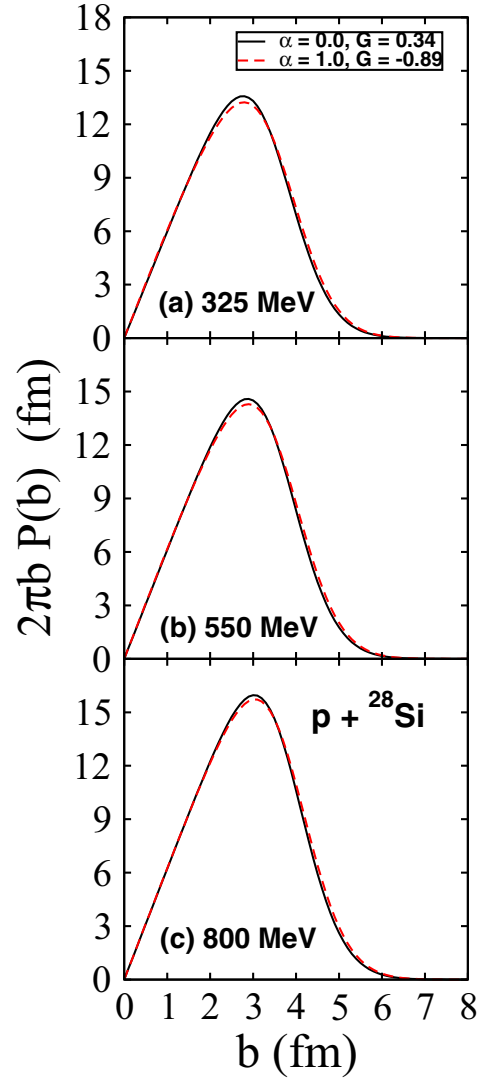

FIG. 2. Reaction probabilities multiplied by $2\pi b$ for proton-^{28}Si reactions at (a) 325, (b) 550, and (c) 800 MeV. The configurations with $\alpha = 0$ ($G = 0.34$) and 1 ($G = -0.89$) are employed.

B. Bubble structure in proton-^{28}Si reactions

How are the different density profiles displayed in Fig. 1 reflected in the reaction observables? To address this question, we calculated the reaction probability $P(b)$ given in Eq. (5), which is the integrand of the total reaction cross section [Eq. (4)]. Figure 2 shows the reaction probability multiplied by $2\pi b$ for proton-^{28}Si scattering as a function of the impact parameter. The density distributions with $\alpha = 0$ (d dominance, $G = 0.34$) and 1 (maximum s configuration, $G = -0.89$) are examined to see the difference between the two extreme configurations. The reaction probabilities for these configurations are almost identical at small impact parameters up to ≈ 2 fm despite the fact that these two density profiles show significant difference in Fig. 1. Since the nucleon-nucleon interaction is large enough, the reaction occurs almost entirely in the internal region below the nuclear radius, as predicted by the black sphere model, which explains high-energy
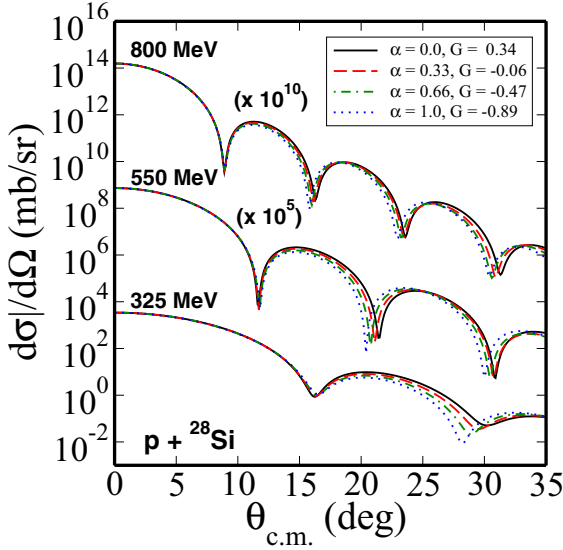
FIG. 3. Elastic scattering differential cross sections of proton-^{28}Si reactions at 325, 550, and 800 MeV with various bubble parameters.

proton-nucleus scattering fairly well [28–30]. Therefore, it cannot directly probe the internal part of the nuclear density profile.

However, we see some differences beyond $b \approx 2$ fm at the nuclear surface, which suggests the possibility of extracting the surface information from the cross sections. In fact, the relation between elastic scattering differential cross sections and nuclear surface diffuseness has been discussed in Ref. [31] and recently in Ref. [23]. It was shown that the smaller the nuclear diffuseness is, the larger is the cross section at the peak position of the first diffraction. Note that the bubble density distribution has smaller diffuseness than the nonbubble density distribution as seen in Fig. 1, because the former ($\alpha = 0$) includes only the d-wave configuration, while the latter ($\alpha = 1$) includes the $1s$ configuration which has a longer tail in the asymptotic region. Consequently, we expect that the bubble structure gives the larger cross section at the first diffraction peak.

To confirm this numerically, we calculated the proton-^{28}Si elastic scattering differential cross sections. Figure 3 plots the elastic scattering differential cross sections of proton-^{28}Si reactions at 325, 550, and 800 MeV with various bubble parameters. As expected, the cross section at the first peak position is largest for the ideal bubble configuration with $\alpha = 0$ and it decreases with increasing α and decreasing G. This suggests a practical way to identify the bubble structure using a hadronic probe.

IV. BUBBLE STRUCTURE OF $N = 14$ ISOTONES

We have seen that the difference between the bubble and nonbubble nuclei can be detected in the elastic scattering differential cross sections. To demonstrate the feasibility of this idea, we take the density distributions obtained from a microscopic structure model, the AMD, and try to extract the

information on the nuclear bubble from the reaction observable. Here the ground-state density distributions of $N = 14$ isotones are examined as they exhibit the bubble structure in its isotone chain [4].

A. Framework of AMD

The AMD [32,33] is a fully microscopic approach and offers a non-empirical description of light to medium nuclei. Here we briefly explain how we obtain the density distributions for the $N = 14$ isotones within the AMD framework. The Hamiltonian for a nucleon system with the mass number A is given by

$$H = \sum_i t(i) - T_{cm} + \sum_{ij} v_{NN}(ij), \qquad (10)$$

where $t(i)$ is the kinetic energy of the ith single nucleon and the center-of-mass kinetic energy T_{cm} is exactly removed. The Gogny D1S parameter set [34] is employed as a nucleon-nucleon effective interaction v_{NN}, which is known to give a fairly good description for this mass region [35–37].

The variational basis function of the AMD is represented by a Slater determinant projected to the positive-parity state as

$$\Phi = \frac{1 + P_x}{2} \mathcal{A}\{\varphi_1, \ldots, \varphi_A\}, \qquad (11)$$

where P_x is the parity operator and φ_i is a Gaussian nucleon wave packet defined by

$$\varphi_i = \prod_{\sigma = x,y,z} \left(\frac{2\nu_\sigma}{\pi}\right)^{1/2} \exp\{-\nu_\sigma (r_\sigma - Z_{i\sigma})^2\}$$
$$\times (\alpha_i \chi_\uparrow + \beta_i \chi_\downarrow)(|p\rangle \text{ or } |n\rangle). \qquad (12)$$

The centroids $\boldsymbol{Z}$ and width $\boldsymbol{\nu}$ vectors of the Gaussian and the spin variables α_i and β_i are the variational parameters. They are determined by the the frictional cooling method [38] in such a way to minimize the energy of the system under the constraint on the quadrupole deformation parameter β.

To describe the ground state of the $N = 14$ isotones, the wave functions obtained by the frictional cooling method are projected to the angular momentum $J = 0$ and superposed employing β as a generator coordinate (generator coordinate method, GCM [39]),

$$\Psi_0 = \sum_i g_i P^{J=0} \Phi(\beta_i), \qquad (13)$$

where $P^{J=0}$ represents the angular momentum projector and the amplitudes g_i are determined by the diagonalization of the Hamiltonian. In the present study, the value of β is chosen from 0.0 to 0.6 with an interval of 0.025. The deformation parameter γ is determined variationally, and hence it takes an optimal value for each $\Phi(\beta_i)$. Finally, the ground-state density distribution is calculated as

$$\rho(\boldsymbol{r}) = \frac{\langle \Psi_0 | \sum_{i=1}^A \delta^3(\boldsymbol{r}_i - \boldsymbol{r}_{cm} - \boldsymbol{r}) | \Psi_0 \rangle}{\langle \Psi_0 | \Psi_0 \rangle}. \qquad (14)$$

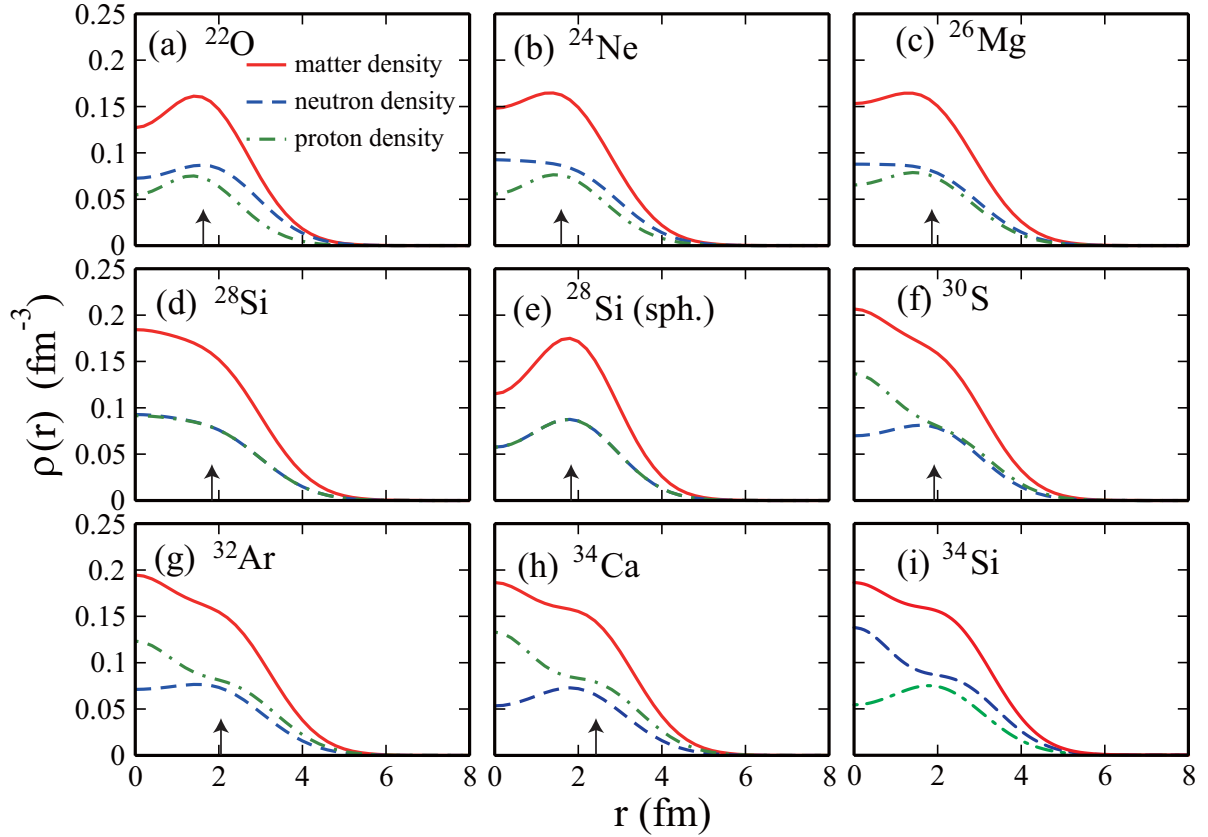Note that the resulting density distribution is free from the center-of-mass coordinate $\boldsymbol{r}_{cm}$. We also evaluate

FIG. 4. Density distributions of $N = 14$ isotones (a) ^{22}O, (b) ^{24}Ne, (c) ^{26}Mg, (d) ^{28}Si, (e) ^{28}Si (spherical), (f) ^{30}S, (g) ^{32}Ar, and (h) ^{34}Ca obtained from the AMD wave function. The arrows indicate the reference radii for each isotone. See text for details. The density distribution of ^{34}Si which is the mirror nucleus of ^{34}Ca and has prominent proton bubble structure is also shown in panel (i) for comparison.

the quadrupole deformation parameters and occupation probabilities of the $1s$ orbit according to the procedure described in the Appendix.

B. Density distributions of $N = 14$ isotones

Figure 4 plots the matter, neutron, and proton density distributions of $N = 14$ isotones obtained with the AMD. The rms matter radii, quadrupole deformation parameters, and occupation probabilities of the $1s$ orbit are summarized in Table I. The bubble parameters G_{AMD} were also calculated from the AMD densities using Eq. (9), where the reference radius (D), for each isotone, was derived from an effective density $\rho^d(r)$. This $\rho^d(r)$ is essentially a HO density [as in Sec. (III A)] whose size parameter is adjusted so as to reproduce the rms matter radius, for each isotone, as obtained from the AMD density.

We clearly see a prominent bubble structure in ^{22}O in which both the proton and neutron density distributions exhibit depressed central densities. Consequently, it has the largest bubble parameter among the $N = 14$ isotones. This is due to the almost spherical closed-shell configuration of this nucleus and the resultant small occupation probabilities of the $1s$ orbit. As the proton number increases, the nuclear quadrupole deformation becomes strong, which mixes the s, d, and g orbits and effectively increases the occupation

probabilities of the $1s$ orbit. As a result, the bubble structure in the matter density distributions is weakened in ^{24}Ne and ^{26}Mg, and diminished in ^{28}Si which is most strongly deformed among the $N = 14$ isotones. Indeed, Table I shows that the bubble parameter strongly correlates with the quadrupole deformation parameter β and neutron occupation probability $P_{1s}(n)$. The bubble parameter decreases as a function of the proton number and becomes negative (nonbubble) from ^{28}Si.

TABLE I. rms matter radii r_m and the quadrupole deformation parameters β, γ, and neutron (proton) occupation probabilities of the $1s$ orbit, $P_{1s}(n)$ $[P_{1s}(p)]$, for $N = 14$ isotones obtained by the AMD. The bubble parameters G_{AMD} are extracted from the matter density distributions shown in Fig. 4. See text for more details.

	r_m (fm)	β	γ	$P_{1s}(n)$	$P_{1s}(p)$	G_{AMD}
^{22}O	2.90	0.20	$60°$	0.21	0.01	0.21
^{24}Ne	2.97	0.37	$60°$	0.28	0.01	0.09
^{26}Mg	3.06	0.40	$37°$	0.26	0.05	0.04
^{28}Si	3.11	0.40	$60°$	0.29	0.29	-0.16
^{28}Si (sph.)	2.98	0.00		0.01	0.01	0.34
^{30}S	3.11	0.27	$43°$	0.17	0.65	-0.29
^{32}Ar	3.21	0.27	$60°$	0.21	0.62	-0.25
^{34}Ca	3.26	0.12	$60°$	0.06	0.91	-0.05

We also see that, if we restrict the AMD calculation to spherical shape, ^{28}Si also shows the bubble structure, as displayed in Fig. 4(e). This confirms a strong impact of the nuclear deformation on the bubble structure. With further increase of the proton number, in ^{30}S, ^{32}Ar, and ^{34}Ca the bubble structure in the matter density distributions is not seen since the central densities of protons are already filled by the excess protons, while the neutron density distributions still keep the bubble structure.

Thus, the present AMD calculation suggests that ^{22}O has both proton and neutron bubble structure. We note, however, this is in contradiction to the conclusion of the mean-field calculations [4]. It was shown that the bubble structure of ^{22}O is rather model dependent, and pairing correlation tends to diminish the bubble structure as it increases the neutron occupation of the $1s$ orbit. Since the present AMD calculation does not handle the pairing correlation explicitly, the stability of the bubble structure of ^{22}O shown in Fig. 4 needs to be investigated. To check the reliability of the AMD densities, we calculated the mirror nucleus of ^{34}Ca, i.e., ^{34}Si, for which many calculations predicted proton bubble structure [4,40] and indirect experimental evidence was obtained [14]. The calculated density shown in panel (i) of Fig. 4 clearly exhibits the proton bubble structure, which is very similar to that of ^{34}Ca and also to that obtained by the mean-field calculations [4]. Therefore, we conclude that the proton (neutron) bubble structure of ^{34}Si (^{34}Ca) is robust, while the bubble structure of ^{22}O is somewhat model dependent.

V. DISCUSSIONS

A. Extraction of bubble parameters for $N = 14$ isotones

In the previous section, we saw that $N = 14$ isotones show remarkable variations in their nuclear density profiles, with ^{22}O exhibiting the most prominent bubble structure, although strong model dependence was reported [4]. We now examine the possibility of extracting the degree of the bubble structure from the reaction observables by performing a numerical test as follows. First, we calculate the elastic scattering differential cross sections using the density distributions obtained by the AMD, which we regard as the experimental data (mock-up data). Then, by assuming spherical HO type density distributions defined in Eq. (8), we fit the α (the mixing parameter) and size parameter of the HO to reproduce the position and magnitude of the first diffraction peak of the mock-up data. This procedure uniquely determines the spherical HO type density distribution from which we extract the bubble parameter G. Thus, the obtained bubble parameter G is compared with that of the original one, G_{AMD} listed in Table I, to test the feasibility of the method.

Figure 5 plots the bubble parameters of $N = 14$ isotones obtained from the mock-up data at the incident energies of 325, 550, and 800 MeV, in comparison with G_{AMD}. It is noted that all the mock-up data (total reaction cross sections calculated with AMD densities) are reproduced within 1% differences. The differences of the extracted bubble parameters are also less than 1% for all the incident energies. These show the robustness of this analysis. Although the bubble
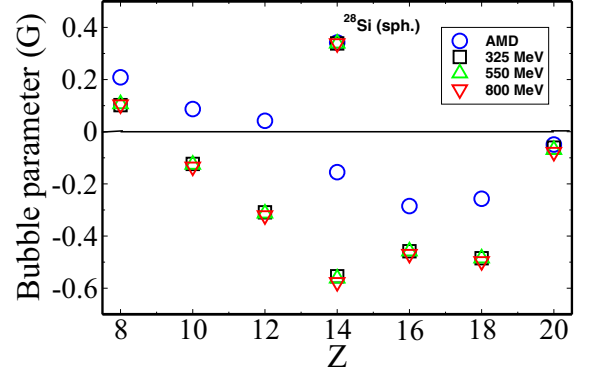

FIG. 5. Comparison of the bubble parameters obtained directly from the AMD densities and the elastic scattering analysis at the incident energies of 325, 550, and 800 MeV.

parameters extracted from the elastic scattering cross sections always undershoot the "exact" bubble parameters G_{AMD} (overestimate the bubble structure), we do notice similarity in their behavior as a function of the proton number. The disagreement is apparently due to the inappropriate assumption of the model density; we assumed spherical HO density distributions for all $N = 14$ isotones. However, most of the nuclei are deformed, inducing some deviations in the bubble parameter extraction. In fact, as we see in Fig. 5, the bubble parameter of ^{28}Si is perfectly reproduced when we constrain the AMD calculation to the spherical configuration. We also see a reasonable description of almost spherical nuclei, ^{22}O ($Z = 8$) and ^{34}Ca ($Z = 20$). Although it is beyond the scope of this paper, an analysis with more elaborated model density distributions including such as nuclear deformation is worth considering to obtain more precise determination of the bubble parameters.

B. How effective is proton scattering in probing the nuclear bubble?

One may think that proton scattering does not probe the nuclear bubble structure but only probes the nuclear surface regions, the nuclear diffuseness. To address this self-criticism, we performed the same analysis as in the previous section but with the two-parameter Fermi (2pF) model density, $\rho_0/[1 + \exp{(r - R)/a}]$, whose parameters (R, a) are fixed so as to reproduce the first peak position and its magnitude in the elastic scattering differential cross sections. ρ_0, the central density, gets fixed from the normalization of the density distribution. Obviously, the 2pF distribution has no bubble. Note that with this analysis the 2pF model density nicely reproduced the density profile near the nuclear surface of the realistic density distributions obtained from the microscopic mean-field model [23].

Figure 6 displays the proton-^{22}O elastic scattering differential cross sections with the AMD, HO, and 2pF model densities as a function of the four-momentum transfer $|-t|$ at the incident energies of 325, 550, and 800 MeV. The cross sections are essentially the same up to $|-t| \approx 3$ GeV/c, which is understandable as both the HO and 2pF model densities are
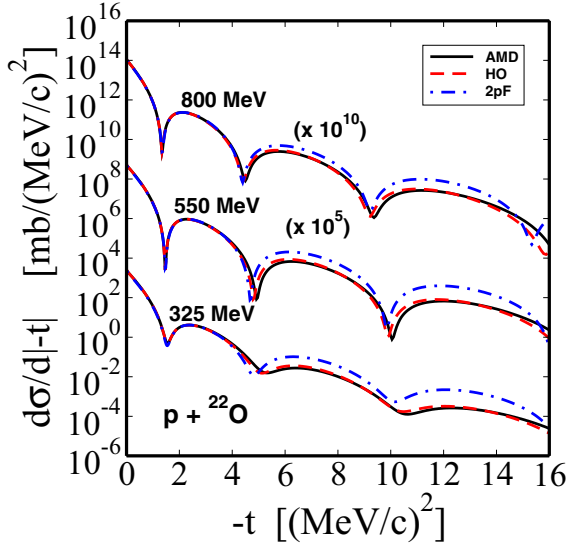
FIG. 6. Elastic scattering differential cross sections of $p + {}^{22}$O with the AMD, HO, and 2pF densities.

adjusted to reproduce the position and magnitude of the first diffraction peak. However, beyond this limit, while the HO and AMD results agree with each other, those with the 2pF model density deviate significantly.

We already know from Fig. 2 that the incident proton cannot probe differences in the internal densities below ≈2 fm. The difference of the density profiles in the middle to the surface regions, in which the bubble structure is still not masked, can be distinguished by analyzing the cross sections in the backward angles beyond the first peak. The proton-nucleus scattering can indeed be an effective tool to probe the bubble structure in exotic nuclei. We remark that a similar indication was found in the analysis of proton-^{48}S scattering with bubble and nonbubble density profiles [41].

VI. CONCLUSIONS

Nuclei with a depression in the central part of their density—the so-called bubble structure—have attracted attention in recent times. Considerable efforts are under way to look for suitable probes for these exotic systems. In this work, we have discussed the feasibility of using a proton probe to extract the degree of the bubble structure. We have calculated the structure of even-even $N = 14$ isotones in the $22 \leqslant A \leqslant 34$ mass range using a microscopic structure model, the antisymmetrized molecular dynamics (AMD). The Glauber model is then employed to evaluate reaction observables of high-energy nucleon-nucleus scattering.

Due to the strong absorption in the internal region of the target nucleus, the bubble structure or the central depression of the target density cannot be directly measured using the proton probe. However, effects of this structure are reflected from the middle to the surface regions of the nuclear density. They also tend to have a sharper nuclear surface. Furthermore,

nuclear deformation acts as an hindrance to the emergence of the bubble structure.

We find that the AMD calculation predicts prominent bubble structure of ^{22}O, which exhibits a small deformation, after analyzing a host of $N = 14$ isotones. The degree of the bubble structure is extracted by a systematic analysis of the calculated cross sections obtained with the AMD by using simple harmonic-oscillator type model densities. To improve the accuracy of the extraction, it is necessary to employ a more realistic model density that can describe the nuclear deformation.

We have shown that the bubble structure information is imprinted on the nucleon-nucleus elastic scattering differential cross sections and is possibly extracted by analyzing the cross sections up to the first diffraction peak. Nevertheless a more accurate analysis involving the second diffraction peak would be a welcome addition.

APPENDIX: ESTIMATION OF THE DEFORMATION PARAMETERS AND OCCUPATION PROBABILITIES FROM THE AMD WAVE FUNCTIONS

Here, we explain how we estimated the quadrupole deformation parameters and single-particle occupation probabilities of the AMD wave functions for $N = 14$ isotones listed in Table I. The AMD wave function given in Eq. (13) is, in general, a superposition of the Slater determinants with different deformation and different single-particle configurations. Therefore, to estimate these quantities, we pick up the Slater determinant $\Phi(\beta)$, which has the maximum overlap with the AMD wave function $|\langle P^{J=0}\Phi(\beta)|\Psi_0\rangle|$, and regard it as an approximation of the AMD wave function Ψ_0.

The deformation parameters β and γ of Ψ_0 may be approximated by those of $\Phi(\beta)$. The occupation probabilities of the $1s$ orbit are also estimated in a similar manner. We calculate the single-particle orbits of $\Phi(\beta)$ by using the AMD+HF method [42]. Because of the nuclear deformation, the single-particle orbits, $\phi_1(\boldsymbol{r}), \ldots, \phi_A(\boldsymbol{r})$, are no longer the eigenstates of the angular momentum. Therefore, we consider the multipole decomposition of them,

$$\phi_i(\boldsymbol{r}) = \sum_{jlj_z} \phi_{i;jlj_z}(r)[Y_l(\hat{r}) \times \chi_{1/2}]_{jj_z}. \quad \text{(A1)}$$

The squared amplitudes for the $j = 1/2$ and $l = 0$ components should give us an estimate of the occupation probability. Assuming the complete filling of the $0s$ orbit, the neutron (n) and proton (p) occupation probabilities of the $1s$ orbit are obtained approximately as

$$P_{1s}(n/p) = \sum_{i=1}^{N/Z} \sum_{j_z=-\frac{1}{2}}^{\frac{1}{2}} \left| \left\langle \phi_{i;\frac{1}{2}0j_z} \middle| \phi_{i;\frac{1}{2}0j_z} \right\rangle \right|^2 - 2. \qquad (A2)$$

[1] I. Tanihata, H. Hamagaki, O. Hashimoto, Y. Shida, N. Yoshikawa, K. Sugimoto, O. Yamakawa, T. Kobayashi, and N. Takahashi, Phys. Rev. Lett. **55**, 2676 (1985).

[2] I. Tanihata, H. Savajols, and R. Kanungo, Prog. Part. Nucl. Phys. **68**, 215 (2013).

[3] R. Hofstadter, Rev. Mod. Phys. **28**, 214 (1956).

[4] M. Grasso, L. Gaudefroy, E. Khan, T. Nikšić, J. Piekarewicz, O. Sorlin, N. Van Giai, and D. Vretenar, Phys. Rev. C **79**, 034318 (2009).

[5] J. J. Li, W. H. Long, J. L. Song, and Q. Zhao, Phys. Rev. C **93**, 054312 (2016).

[6] X. Campi and D. W. L. Sprung, Phys. Lett. B **46**, 291 (1973).

[7] K. T. R. Davis, S. J. Krieger, and C. Y. Wong, Nucl. Phys. A **216**, 250 (1973).

[8] E. Khan, M. Grasso, J. Margueron, and N. Van Giai, Nucl. Phys. A **800**, 37 (2008).

[9] G. Co', M. Anguiano, V. De Donno, and A. M. Lallena, Phys. Rev. C **97**, 034313 (2018), and references therein.

[10] G. Saxena, M. Kumawata, B.-K. Agrawal, and M. Aggarwal, Phys. Lett. **789**, 323 (2019).

[11] G. Saxena, M. Kumawata, B.-K. Agrawal, and M. Aggarwal, J. Phys. G: Nucl. Part. Phys. **46**, 065105 (2019).

[12] M. Bender, K. Rutz, P.-G. Reinhard, J. A. Maruhn, and W. Greiner, Phys. Rev. C **60**, 034304 (1999).

[13] B. Schuetrumpf, W. Nazarewicz, and P.-G. Reinhard, Phys. Rev. C **96**, 024306 (2017), and references therein.

[14] A. Mutschler, A. Lemasson, O. Sorlin, D. Bazin, C. Borcea, R. Borcea, Z. Dombrádi, J.-P. Ebran, A. Gade, H. Iwasaki *et al.*, Nat. Phys. **13**, 152 (2017).

[15] K. Tsukada, A. Enokizono, T. Ohnishi, K. Adachi, T. Fujita, M. Hara, M. Hori, T. Hori, S. Ichikawa, K. Kurita *et al.*, Phys. Rev. Lett. **118**, 262501 (2017).

[16] S. Abrahamyan *et al.* (PREX Collaboration), Phys. Rev. Lett. **108**, 112502 (2012).

[17] H. Sakaguchi and J. Zenihiro, Prog. Part. Nucl. Phys. **97**, 1 (2017), and references therein

[18] Y. Matsuda, H. Sakaguchi, H. Takeda, S. Terashima, J. Zenihiro, T. Kobayashi, T. Murakami, Y. Iwao, T. Ichihara, T. Suda *et al.*, Phys. Rev. C **87**, 034614 (2013).

[19] R. J. Glauber, in *Lectures in Theoretical Physics*, edited by W. E. Brittin and L. G. Dunham (Interscience, New York, 1959), Vol. 1, p. 315.

[20] K. Varga, S. C. Pieper, Y. Suzuki, and R. B. Wiringa, Phys. Rev. C **66**, 034611 (2002).

[21] T. Nagahisa and W. Horiuchi, Phys. Rev. C **97**, 054614 (2018).

[22] B. Abu-Ibrahim, S. Iwasaki, W. Horiuchi, A. Kohama, and Y. Suzuki, J. Phys. Soc. Jpn. **78**, 044201 (2009).

[23] S. Hatakeyama, W. Horiuchi, and A. Kohama, Phys. Rev. C **97**, 054607 (2018).

[24] L. Ray, Phys. Rev. C **20**, 1857 (1979).

[25] W. Horiuchi, Y. Suzuki, B. Abu-Ibrahim, and A. Kohama, Phys. Rev. C **75**, 044607 (2007).

[26] B. Abu-Ibrahim, W. Horiuchi, A. Kohama, and Y. Suzuki, Phys. Rev. C **77**, 034607 (2008); **80**, 029903(E) (2009); **81**, 019901(E) (2010).

[27] I. Angeli and K. P. Marinova, At. Data Nucl. Tables **99**, 69 (2013).

[28] A. Kohama, K. Iida, and K. Oyamatsu, Phys. Rev. C **69**, 064316 (2004).

[29] A. Kohama, K. Iida, and K. Oyamatsu, Phys. Rev. C **72**, 024602 (2005).

[30] A. Kohama, K. Iida, and K. Oyamatsu, J. Phys. Soc. Jpn. **85**, 094201 (2016).

[31] R. D. Amado, J. P. Dedonder, and F. Lenz, Phys. Rev. C **21**, 647 (1980).

[32] Y. Kanada-Enyo, M. Kimura, and H. Horiuchi, C. R. Phys. **4**, 497 (2003).

[33] M. Kimura, Phys. Rev. C **69**, 044319 (2004).

[34] J. Berger, M. Girod, and D. Gogny, Comput. Phys. Commun. **63**, 365 (1991).

[35] T. Sumi, K. Minomo, S. Tagami, M. Kimura, T. Matsumoto, Y. R. Shimizu, and M. Yahiro, Phys. Rev. C **85**, 064613 (2012).

[36] S. Watanabe, K. Minomo, M. Shimada, S. Tagami, M. Kimura, M. Takechi, M. Fukuda, D. Nishimura, T. Suzuki, T. Matsumoto, Y. R. Shimizu, and M. Yahiro, Phys. Rev. C **89**, 044610 (2014).

[37] S. Pèru and M. Martini, Eur. Phys. J. A **50**, 88 (2014).

[38] Y. Kanada-Enyo, M. Kimura, and A. Ono, Prog. Theor. Exp. Phys. **2012**, 01A202 (2012).

[39] D. L. Hill and J. A. Wheeler, Phys. Rev. **89**, 1102 (1953).

[40] T. Duguet, V. Somà, S. Lecluse, C. Barbieri, and P. Navrátil, Phys. Rev. C **95**, 034319 (2017).

[41] T. Furumoto, K. Tsubakihara, S. Ebata, and W. Horiuchi, Phys. Rev. C **99**, 034605 (2019).

[42] A. Dote, H. Horiuchi, and Y. Kanada-En'yo, Phys. Rev. C **56**, 1844 (1997).